Electrochimica Acta 296 (2019) 1083–1094

Contents lists available at ScienceDirect

Electrochimica Acta

journal homepage: www.elsevier.com/locate/electacta

Hydrothermally synthesised NiCoP nanostructures and electrospun N-doped carbon nanofiber as multifunctional potential electrode for hybrid water electrolyser and supercapatteries

Subramani Surendran [a], Sathyanarayanan Shanmugapriya [a], Pei Zhu [b], Chaoyi Yan [b], Ramasamy Hari Vignesh [c], Yun Sung Lee [c], Xiangwu Zhang [b, **], Ramakrishnan Kalai Selvan [a, b, *]

[a] Energy Storage and Conversion Devices Laboratory, Department of Physics, Bharathiar University, Coimbatore, 641-046, Tamil Nadu, India
[b] Department of Textile Engineering, Chemistry and Science, North Carolina State University, Raleigh, NC 27695-8301, USA
[c] Faculty of Applied Chemical Engineering, Chonnam National University, Gwangju, 500-757, South Korea

ARTICLE INFO

Article history:
Received 18 September 2018
Received in revised form
11 November 2018
Accepted 11 November 2018
Available online 14 November 2018

Keywords:
Supercapattery
Water electrolyzer
Electrospinning
Phosphides
Carbon nanofiber

ABSTRACT

In this work, a facile single-step hydrothermal technique is used to prepare a spherically concomitant foamy NiCoP as positrode for supercapatteries. Similarly, the nitrogen-doped carbon nanofibers are prepared by simple electrospinning technique to use as negatrode. The prepared materials are raptly examined through primary studies for both energy conversion and storage applications. Fascinatingly, NiCoP electrode encourages oxygen evolution reaction, and the carbon nanofiber electrode emboldens hydrogen evolution reaction with the minimum overpotential of 257 mV and 160 mV, respectively. In addition, a supercapattery is designed and operated at a full voltage window of 1.6 V using the fusion of carbon nanofiber as the negatrode and the cutting-edge NiCoP as the positrode, which presents a superior energy (56 Wh kg^{-1}) and an improved power density (5333 W kg^{-1}) with a long cyclic stability (5000 cycles). Finally, the fabricated supercapattery device is used to power the constructed hybrid water electrolyser that requisites a low cell voltage of 1.71 V to afford a current density of 10 mA cm^{-2}. Overall, the prepared electrodes reveal its superiority of handling the multifunctional challenges for both water electrolyzer and supercapatteries.

1. Introduction

The discovery and production of exceedingly cheap and proficient energy conversion and storage (ECS) systems are in full swing to meet the future energy needs. Budding researchers are in an exciting context to sense and sight an electrode material that justifies all the multifunctional necessities to promote an economically thriving ECS system. Accordingly, the water electrolyser is ensnaring a great deal of interest as an energy conversion approach as it uses prompting renewable and clean energy resources to replace the use of limited fossil fuels [1]. The oxygen and hydrogen evolution reaction functions as pivotal points of reference for the on-demand water electrolysers [1,2]. The operational efficiencies of OER and HER reactions are explicitly reliant on their catalysts. Habitually, ruthenium or iridium-based noble metals are employed as efficient electrocatalysts to promote the OER while the noble platinum-based electrodes are engaged as active electrocatalysts for the HER [3]. The relatively high price, as well as the limited resources of these noble metals, restrict the commercial competence of this application. Hence, swapping these noble metals by non-noble or metal-free electrocatalysts with improved catalytic activity is an effective way to loom this system in large-scale applications. Earlier, transition metal-based hydroxides and oxides were vastly investigated as an imminent bifunctional electrocatalyst to promote both the OER and HER activities [4]. However, the sluggish kinetic rate engendered by these materials massively affected its OER and HER catalytic activity [5].

* Corresponding author. Energy Storage and Conversion Devices Laboratory, Department of Physics, Bharathiar University, Coimbatore, 641-046, Tamil Nadu, India.
** Corresponding author.
E-mail addresses: xzhang13@ncsu.edu (X. Zhang), selvankram@buc.edu.in (R.K. Selvan).

https://doi.org/10.1016/j.electacta.2018.11.078
0013-4686/

Similarly, the electrochemical capacitors or supercapacitors are making a high impact as a prospect of proficient energy storage approach, which delivers a high power density with the rapid rate of charging and discharging, extended life, high safety, and sustainability [6]. Although supercapacitors are a proficient energy storage system, concerns are outstretched over its marginally shaky energy density to encounter the commercial scenarios. With the aim of recovering this energy density insufficiency, a flexible supercapattery was fabricated, which capable of delivering excellent power density in conjunction with boosted energy density. The supercapattery devices are sprouting to be a dominant energy source by the execution of a non-Faradaic electric double layer capacitor (EDLC)-type electrode as an anode (negatrode) and the Faradaic battery-type electrode as a cathode (positrode) [7]. Here, the carbon-based materials are used as EDLC electrodes which indeed provide excellent power density while the transition metal-based electrodes are ensuring enhanced energy density.

In prospect of a developed multifunctional electrode material including oxides [8], hydroxides [9], double hydroxides [10], sulphides [11] and phosphides [12], bimetallic phosphides are receiving great deal of attention owing to its unusual properties especially the introduction of hetero-metal ions shows synergistic effect that ensures rich redox sites and further improves the electrochemical conductivity and stability. Moreover, the single metal phosphides suffer either poor cycling stability or relatively low specific capacitance which is found to get counterbalanced with the bimetallic phosphides [13–15]. Among these, the ternary NiCoP is far superior to the binary phosphides (Ni-P & Co-P) due to its enhanced crystallinity, upgraded electronic configuration and improved electrical conductivity by stimulating electrochemical properties, holding high eco-friendly properties [16]. The bimetallic phosphide is envisioned to prove itself as a highly active and durable electrocatalyst towards OER since the synergistic effect of two metals with more active sites, and control the intrinsic electrical properties of the bimetallic compound. Specifically, Li et al. have grown NiCoP nanowire arrays on 3D Ni foam by a two-step method enabled the electrocatalysts with remarkable electrocatalytic performance and stability (28 h) for OER (370 mV) and HER (197 mV) [17]. Similarly, Du et al. have provided a sequential hydrothermal, oxidation, and phosphatization technique to develop a three-dimensional NiCoP/carbon cloth electrocatalyst that has yielded a current density of 10 mA cm^{-2} at 1.52 V [16]. Likewise, Liang et al. presented a PH_3 plasma-assisted approach to convert NiCo hydroxides into ternary NiCoP, which was used as both cathode and anode for overall water splitting and a current density of 10 mA cm^{-2} was achieved at a cell voltage of 1.58 V [18]. Correspondingly, Yu et al., has prepared NiCoP films with different nickel-to-cobalt ratios by an electrodeposition technique that exhibited the best state-of-the-art performance with a voltage of 1.57 V, delivering 10 mA cm^{-2} in a two-electrode electrolyzer [19]. Also, Li et al. have reported Co-doped nickel phosphides ($Ni_{2-x}Co_xP$) and their hybrids with reduced graphene oxide (rGO) as bifunctional electrocatalysts for HER (42 mV) and OER (270 mV) [20].

Considering the supercapacitor applications, Liang et al. have reported the electrochemical performance of the asymmetric supercapacitor devices based on the NiCoP nanoplates and graphene films, which delivered a high energy density of 32.9 Wh kg^{-1} at a power density of 1301 W kg^{-1} [21]. Likewise, Kong et al. demonstrated NiCoP/NF prepared by the phosphorization of hydrothermally obtained $NiCo(OH)_xF$/NF, which delivered a high energy density of 1.16 mWh cm^{-2} at a power density of 1.6 mWcm^{-2} [22]. Similarly, Wang et al. prepared NiCoP/G hybrid electrode which has shown excellent electrochemical properties with a specific capacitance of 646 F g^{-1} at 4 A g^{-1} and maintained 91% of this initial capacitance after 2000 cycles [23]. Also, Hu et al. have proposed bimetallic nickel cobalt phosphides with high electrical conductivity and different Ni/Co molar ratios, and achieved a high energy density of 32 Wh kg^{-1} at a power density of 0.351 kW kg^{-1} [24]. Previously, we have reported the multifunctional applications of NiCoP embedded CNF prepared by single step electrospinning method [25]. On the other hand, in the present work, we have prepared the NiCoP by the simple hydrothermal method.

Besides, the nanostructured carbon materials, with its distinguished demand, exist in various forms such as carbon/graphene quantum dots, carbon nanofiber (CNFs), carbon nanotubes (CNTs), graphene, carbon nanosheets, 3D carbon nanostructures, porous carbon and carbon nanorods (CNRs) [26,27]. Among them, CNFs are peculiarly renowned because of its intrinsic advantages, such as the large surface area, lightweight, good electrical conductivity, and high thermal/chemical/mechanical stability, which all make CNFs to be a perceptible contender in numerous electrochemical applications [26,27]. Additionally, heteroatoms doping has been proved to be an effective way to functionalised CNFs as working electrodes in the electrochemical applications such as supercapacitors, Li-ion batteries and Li-air batteries [28]. Besides, they can also be used as efficient electrocatalysts in water electrolysis, oxygen reduction reaction and CO_2 reduction [29]. Hence the functionalised CNFs and the promoted ternary NiCoP are grasping a huge deal of impact over the prospect of the ECS systems.

Even though bimetallic NiCoP has been emerging as a noteworthy electrocatalyst, these NiCoP electrocatalysts were prepared via multifaceted two-step synthesis encompassing high-temperature treatment, which increased the production cost that foiled the large-scale commercialization. Therefore, this work emphasizes the facile single-step hydrothermal technique to fabricate unique bimetallic spherically concomitant foamy NiCoP (SCFN) nanostructures to divulge as an efficient OER electrocatalyst and a supercapattery electrode. As well as the nitrogen-doped CNF electrocatalysts with its massively subjugated active catalytic sites and unique surface chemistry functionalities delivered a superior HER activity. As a final point, the fabricated supercapattery was integrated with the assembled hybrid water electrolyser (SCFN||N-CNF) and the performance was studied.

2. Experimental section

2.1. Preparation of SCFN as positrode

Stoichiometric amounts of nickel nitrate (Merck), cobalt nitrate (Merck) and red phosphorus (Alfa Aesar) were dispersed in a medium of double distilled water (40 ml), and the solution was left under stirring for 10 min. The homogeneous mixture was then transferred to the Teflon-lined autoclave and maintained at 160 °C for 24 h to obtain a black product which was centrifuged, and dried at 80 °C under vacuum. The collected NiCoP sample was subjected to various structural and surface-associated studies.

2.2. Preparation of N-CNF as negatrode

Polyacrylonitrile (2.4 g) was dissolved into 30 g N-dimethylformamide under unceasing mechanical stirring for 24 h at 80 °C. The attained viscous and homogeneous solution was transferred into a plastic syringe. Successively, the needle-collector distance was optimized to be 15 cm, while the stream rate was adjusted to 0.75 ml/h. Finally, the prepared solution was electrospun into nanofibers under a high voltage of 15 kV. The as-spun nanofibers were first stabilized at 250 °C for 2 h in the air with a heating rate of 5 °C min^{-1}, and then carbonized under a nitrogen atmosphere at 900 °C for 2 h through a heating rate of 2 °C min^{-1}.

The nitrogen atmosphere was used to functionalize the CNF by inoculating hetero atom over the carbon site [30].

2.3. Characterizations techniques

The phase formation and structural analysis were carried out using powder X-ray diffraction (Rint 1000, Rigaku, Japan) with Cu Kα radiation (λ = 1.5418 Å). The morphological features and elemental mapping were evaluated using Field-emission scanning electron microscopy (FE-SEM, S-4700, Hitachi, Japan) coupled with energy-dispersive X-ray spectroscopy (EDX) module, and high-resolution transmission electron microscopy (HR-TEM; JEM-2000, EX-II, JEOL, Japan). The Scion Image software was employed for the particle size measurements and plotting of size distribution histogram. The XPS analysis (Multilab 2000, UK) was performed to determine the oxidation states and chemical bonding between the constituent elements. The Bio-Logic VMP3 multichannel electrochemical workstation was engaged in analysing the electrochemical properties of the samples.

2.4. Electrode preparation

Both the positive and negative electrodes were prepared by brush coating a homogenous slurry containing 8:1:1 ratio of active material (SCFN or N-CNF), carbon black and polyvinylidene difluoride (PVDF) in 0.4 ml of N-methyl 2-pyrrolidine (NMP) on the carbon cloth substrate. The coated electrodes were dried overnight at 80 °C in a vacuum oven. Here, a conventional three-electrode system involving 1 M KOH electrolyte, Hg/HgO reference electrode, and a graphite counter electrode was employed to carry out all the electrochemical measurements. The potentials reported in the electrocatalytic analysis were provided against the RHE (Reversible Hydrogen Electrode). The electrochemical measurements of the supercapattery device were performed using a sealed coin cell (CR2032). The working electrodes were stacked back-to-back within the coin cell with the active material making direct contact with the current collector. The electrolyte used was aqueous 1 M KOH.

3. Results and discussion

3.1. Physicochemical properties of NiCoP positrode

The structural analysis of the prepared NiCoP was characterized by the X-ray diffraction (XRD), and the obtained diffraction pattern is shown in Fig. 1a. The diffraction peaks elucidate the formation of pure hexagonal NiCoP phase with a space group of P-62 m. Besides, no characteristic peaks from other impurities were observed in the XRD pattern, which depicts the high purity of the prepared NiCoP nanostructures. Further, the grain size of the product was estimated using the Scherrer's formula, which is around 27 nm. Also, the lattice constants were calculated from the diffraction data using the CELREF software, which are consistent with the JCPDS card No. 71-2336. The obtained lattice constants are $a = b = 5.8601$ Å, $c = 3.3691$ Å, and the cell volume is $V = 99.19 \times 10^6$ pm^3. Similarly, the calculated structural parameters such as lattice density, the theoretical specific surface area and dislocation density are 7.38 g cm^{-3}, 30.12 m^2 g^{-1} and 1.37×10^{15} lines m^{-2}, respectively. Hence, the prepared SCFN nanoparticles are a pure and highly crystalline phase with enhanced structural parameters of smaller crystallite size and higher theoretical specific surface area.

The X-ray photoelectron spectroscopy (XPS) analysis was

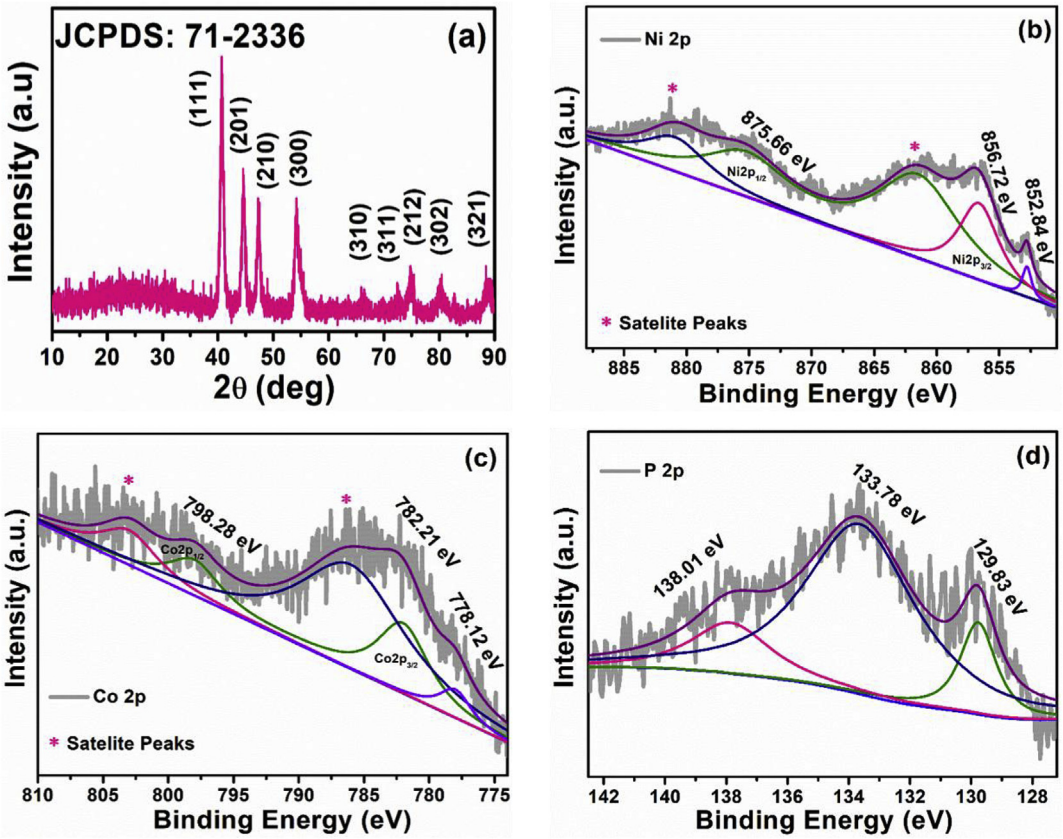

Fig. 1. (a) XRD pattern and (b–c) XPS spectra of SCFN sample.

performed to investigate the surface chemical compositions and valence states of the prepared SCFN sample. The comprehensive core level spectrum of Ni (2p), Co (2p) and P (2p) are shown in Fig. 1b–d, respectively. A peak at a binding energy of 852.84 in the Ni 2p deconvoluted spectrum (Fig. 1b) can be assigned to the Ni-P, which possesses a partial positive charge $Ni^{\delta+}$ than the elemental Ni (852.30 eV). As well as, the two corresponding satellite peaks observed at around 856.72 eV and 875.66 eV can be assigned to the spin-orbital splitting of oxidized Ni species [31]. Similarly, in the Co 2p spectrum (Fig. 1c), a peak at 778.12 eV is positively shifted from the binding energy of elemental Co (777.90 eV), which evidences the partial positive charge of $Co^{\delta+}$ in Co-P compound. Subsequently, the peaks positioned at 798.28 eV and 782.21 eV with their two respective satellite peaks are endorsed by the Co $2p_{1/2}$ and Co $2p_{3/2}$ characteristic peaks of oxidized Co species [19]. In the P 2p spectrum (Fig. 1d), the peak located at 129.83 eV can be consigned to $P^{\delta-}$ in the form of metal phosphide, which is negatively shifted from the elemental P (130.02 eV). Besides, the two broad P-O peaks positioned at 133.78 and 138.01 eV can be ascribed to the phosphate species, formed likely due to the superficial passivation of phosphide particles due to air contact on the surface [32]. Overall it is evident from the energy shifts of Ni, Co and P that there is a small transfer of electron density from the positively charged metals (Ni &Co) to the negatively charged phosphorous [2]. These shifts of binding energies also divulge the shift of the d-band centre relative to the Fermi level, which could decisively facilitate the kinetics of the electrocatalysis [19].

High resolution scanning electron microscopic images of the prepared SCFN is shown in Fig. 2. Fig. 2a shows the uniformly assimilated spherically concomitant nanoparticles of SCFN with a foamy framework. The improved foamy framework has enriched the surface abrasiveness, which influences the creation of active sites that are wide-open to exchange reactions. The calculated particle size of the prepared SCFN was found to be 20-30 nm acquired from the histogram presented in Fig. S1. Also, to improve the vision into the inner structure of SCFN nanoparticles, high-resolution transmission electron microscopy (HR-TEM) characterizations and elemental mapping were carried out. The presence of dark, spherically concomitant, and foamy frameworks of NiCoP (SCFN) nanoparticles was apparently visible in Fig. 2b. The HR-TEM image in Fig. 2c shows distinct lattice fringes with interplanar distances of 0.2 nm, corresponding to the (201) plane of the hexagonal SCFN crystal structure. This further specifies that the bimetallic phosphides are thriving a great possession with respect to the obtained XRD pattern. The SAED pattern in Fig. 2d elucidates the polycrystalline nature of the SCFN nanostructure. Elementally mapped images of SCFN in Fig. 2e–h confirms the composition Ni (cyan), Co (purple), and P (yellow) elements present in the prepared SCFN compound. Further, the domination of the signals substantiates that the Ni, Co and P elements were homogeneously distributed all through the ternary SCFN compound.

3.2. Physicochemical properties of N doped carbon nanofiber as negatrode

Fig. 3a illustrates the HRSEM image of carbonized PAN nanofibers, where the nanofiber structure is precisely discernible. The nanofibers are continuous and have an average diameter of 30 nm, proposing an intertwined assembly. Fig. 3b shows the XRD pattern of the electrospun N-CNF. The XRD profile exhibits two broad diffraction peaks at around 2θ values of 25° and 44°, which are close to the reflections of graphitic planes (002) and (100), respectively. The incidence of a significant peak at 25° unveils the dominant presence of amorphous carbon phase attributing to the low amount of highly crystalline graphitic phase in the CNF. Since the sp^2 hybridized carbon typically enriches the electronic conductivity, the prepared CNF with its dominant carbon phase is expected to provide enhanced electrochemical performance.

The surface chemistry of the prepared CNF was characterized by Raman and X-ray photoelectron spectroscopy. Raman spectrum inferred the degree of structural defects caused by the oxygen and nitrogen moieties within the graphitic planes of the prepared CNF. The analysis of the peak positions and intensities deduce the structural variations in the carbon materials in terms of I_D/I_G ratio. Fig. 3c embodies the typical Raman spectrum of CNFs with two identical peaks, D and G band at 1350 and 1584 cm^{-1}, respectively [33]. The G band can be apportioned to the E_{2g} vibration mode of the hexagonal graphitic lattice, which reveals the presence of well-graphitized carbon while the D band corresponds to the A_{1g} mode that exemplifies the disordered carbon or defective graphitic structures [34]. The I_D/I_G ratio is calculated to be 0.92 in the prepared CNF. This endorses the presence of defects in the carbon lattice introduced by the existence of oxygen and nitrogen-rich functional groups in the CNF.

The XPS analysis stipulates the existence and chemical structure of nitrogen and oxygen atoms on the surface of the carbon nanofibers (Fig. 3d–f). The de-convoluted C 1s spectrum (Fig. 3d) consists of five carbon functional groups namely, graphitic carbon: C-C/

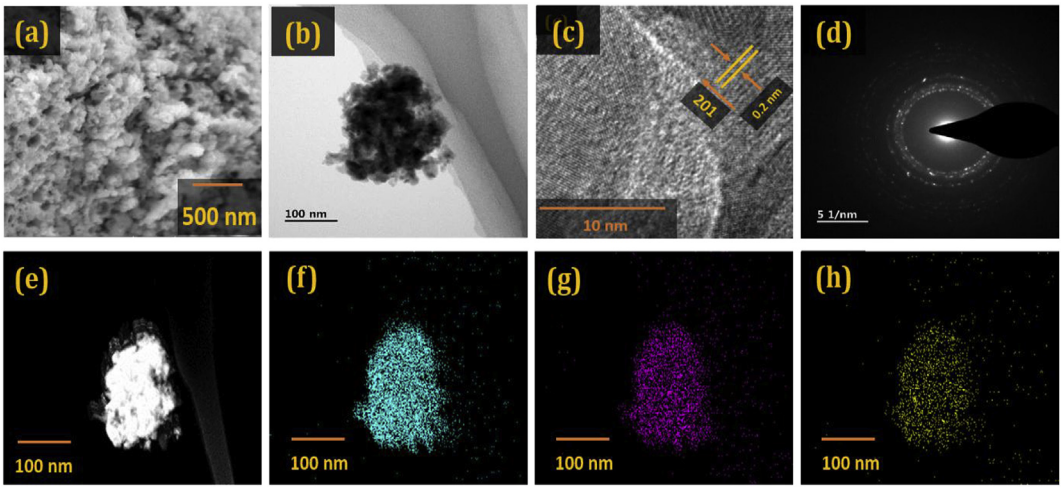

Fig. 2. (a) FESEM image, (b) TEM image, (c) HR-TEM image, (d) SAED pattern, and (e–h) elemental mapping of SCFN.

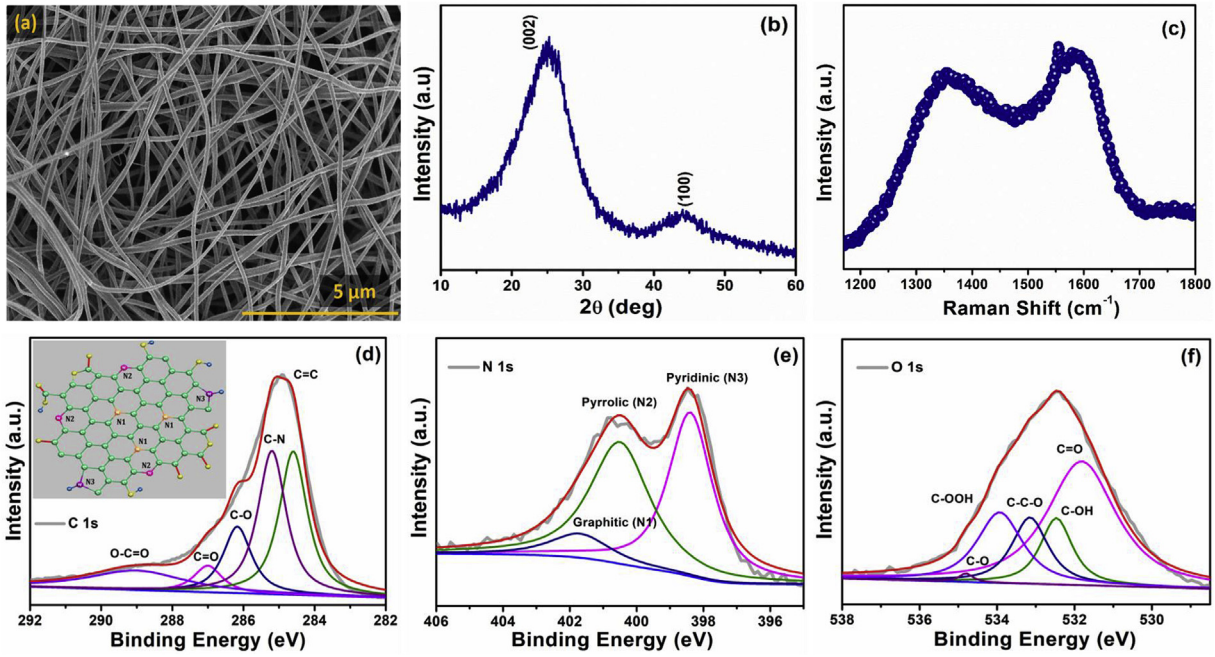

Fig. 3. (a) FESEM image, (b) XRD pattern, and (c) Raman spectrum and (d) C 1s, (e) N 1s and (f) O 1s deconvoluted XPS spectrum of N-CNF sample (inset (d): schematic representation of nitrogen and oxygen functionalities in N-CNF).

C=C (284.85 eV), C-N (285.64 eV), C-O (286.24 eV), C=O (287.45 eV) and O-C=O (289.09 eV) [35]. These peaks of C1s evidences the occupancy of O and N species at the carbon structure. The O 1s core level spectrum as shown in Fig. 3e comprises C=O, C-OH, C-C-O, C-OOH and C-O at the binding energies of 531.88, 532.47, 533.15, 534.03 and 534.80 eV, respectively [36]. The high-resolution spectrum of N 1s (Fig. 3f) is deconvoluted into three significant peaks at the binding energies of 398.44, 400.49 and 401.76 eV corresponding to graphitic (N1), pyridinic (N2) and pyrrolic (N3) species of nitrogen [37]. Inset of Fig. 3d shows the schematic representation signifying the tenancy of various oxygen and nitrogen functionalities in the place of carbon atoms in the prepared CNF. The graphitic nitrogen is sited inside the graphitic carbon plane and bonds with three sp^2 carbon atoms; the pyridinic N alternates a carbon atom in the C6 ring and bonds with two sp^2 carbon atoms and the pyrrolic N in a five-membered ring donates two electrons to the π system [38]. The functional groups can offer carbon materials with an acid/base character that instigate pseudocapacitive Faradaic reaction between the electrolyte ions and the surface functionalities [39]. Among the three N moieties, the pyridinic-N is associated with the pseudocapacitive Faradaic reaction which renders excellent specific capacitance and makes its prevalence more favourable for the supercapacitor applications [40]. Besides, the graphitic nitrogen module existing in the carbon milieu can modify the polarity and electron distribution which could enhance the conductivity of the electrode material [40]. Furthermore, the nitrogen atoms possess lone pair electrons that make them inherently interactive to the reactants (i.e., protons/water) than the carbon atoms. Also, the relatively higher electronegativity of nitrogen than C, render higher positive charge density on their adjacent carbon atoms, on account of which these carbon atoms could become the active catalytic sites [41]. Moreover, the modification of CNFs with oxygen and nitrogen functionalities provide surface defects which act as electrocatalytic active sites and enhance the catalytic activity [36]. Hence the prepared CNFs are expected to thrive hard for both the energy storage and conversion applications.

3.3. Electrocatalytic properties of the electrodes

3.3.1. Oxygen evolution reaction

The electrochemical studies were carried out to identify the electrocatalytic activity of the prepared SCFN and N-CNF electrodes by a conventional three-electrode system, where the proposed electrodes used as working electrode ($1 \times 1\ cm^2$), a graphite rod as an auxiliary electrode ($1 \times 1\ cm^2$) and an Hg/HgO as a reference electrode [42]. The observed potential with respect to Hg/HgO is converted to reversible hydrogen electrode (RHE). The details were given in the supportive information. The OER activities of the prepared electrocatalysts were executed by linear sweep voltammetry (LSV) analysis in 1 M KOH electrolyte at $5\ mV\ s^{-1}$. Fig. 4a shows the LSV curves acquired for the prepared SCFN, N-CNF, commercial carbon cloth, and ruthenium oxide electrocatalyst. The peak observed around 1.2–1.45 V (vs RHE) is endorsed to the oxidation reaction related to the Co^{2+}/Co^{3+} and Ni^{2+}/Ni^{3+} redox couples. The prepared SCFN electrocatalyst has shown a low onset potential of 1.45 V (vs RHE) and has requested an overpotential of 257 mV to attain an elevated current density of $20\ mA\ cm^{-2}$, whereas the prepared N-CNF and commercial RuO_2 electrocatalysts required seemingly high overpotentials of 330 mV and 300 mV to attain a similar current density, respectively. The prepared SCFN electrocatalyst offered a relatively enhanced OER activity compared to the other reported Ni-based electrodes, as listed in Table 1. A tremendous amount of gas bubbles was seen as the potential increased further. Fig. 4b illustrates the required OER overpotential to achieve a current density of $20\ mA\ cm^{-2}$ for all the prepared electrocatalysts. Among the studies systems, the prepared SCFN electrocatalyst performed a better OER catalytic activity than the N-CNF and RuO_2 electrocatalysts.

Fig. 4c shows the Tafel plot for OER electrocatalyst, which is fitted to obtain the Tafel slope [43]. The Tafel slope is used to deduce the rate-determining step in the electrocatalytic system. Here, the SCFN electrocatalyst provides the minimum Tafel slope of 116 mV dec^{-1}, which depicts the single-electron transfer step. According to the literature, the oxy-hydroxide formation is the key intermediate

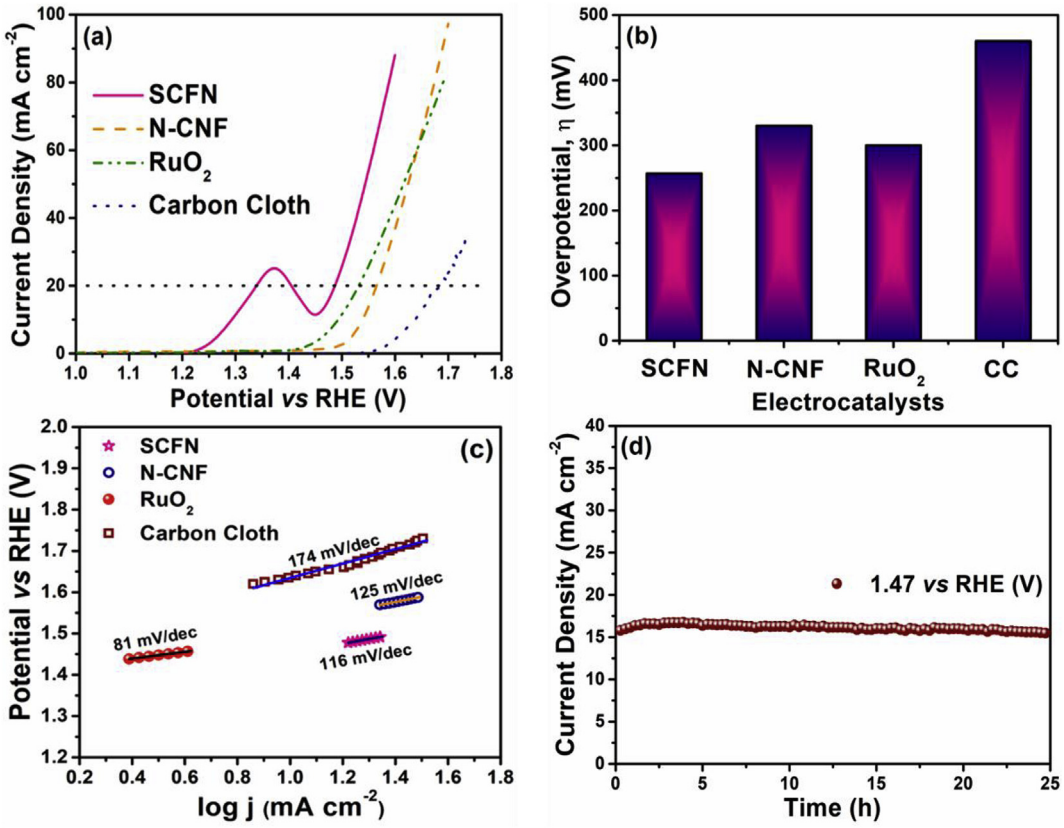

Fig. 4. (a) LSV polarization curves for OER activity, (b) The necessary overpotential to achieve a current density of 20 mA cm^{-2} for different electrocatalysts, (c) Corresponding OER Tafel plots, and (d) Chronoamperometry of SCFN.

Table 1
Comparison of OER and HER performance in 1.0 M KOH with other non-noble-metal electrocatalysts.

Catalyst	Substrate	OER Overpotential [mV] @ 10 mA cm^{-2}	HER Overpotential [mV] @ 10 mA cm^{-2}	Ref.
NiCoP/Ti	Ti	310	102	[6]
Hierarchical NiCoP nanocone arrays	Ni foam	270 @ 20mA	104	[17]
Plasma-Assisted NiCoP	Ni foam	280	32	[18]
$Ni_{0.71}Co_{0.29}P$	Ni foam	341	232	[19]
$Ni_{0.62}Co_{0.38}P$		285	166	
$Ni_{0.51}Co_{0.49}P$		239	82	
$Ni_{0.23}Co_{0.77}P$		265	128	
NiCoP/rGO	Carbon fibre paper	270	209	[20]
NiCoP NW/NF	Ni foam		43	[31]
Nickel Cobalt phosphide nanowires	Ni foam		118	[32]
NiCoP NSA	Ni foam	308 @ 50 mA	133@ 50 mA	[43]
h-CoNiP/rGO	GCE	280		[45]
NiCoP/NC PHCs	GCE	297		[46]
urchin-like NiCoP	GCE		87	[47]
Ni_2P/NiCoP@NCCs	GCE		116	[48]
Ni_2P/NiCoP@NHCCs			168	
NiCoP hollow quasi-polyhedron	GCE		124	[49]
NiCoP		330		[50]
NiCoP-CNTs		320		
SCFN	Carbon cloth	257 @ 20 mA	184	This work
N-CNF	Carbon cloth	330 @ 20 mA	160	This work

for the NiCo-based electrocatalysts and Ni/Co (II) → Ni/Co (III) → Ni/Co (IV) is the most favourable OER mechanism through the formation of β-(Ni/Co)OOH intermediate [20,43]. Fig. 4d shows the chronoamperometry (CA) curve measured at a constant potential of 1.47 V (vs RHE) for 25 h. The negligible changes in the current with the continuous evolution of gas bubbles from the electrode surface corroborates the highly stable nature of the SCFN electrocatalyst for OER activity. The improved OER catalytic activity of the SCFN sample can be ascribed to the concurrence of the two utmost electrochemically active transition metals Ni and Co in the phosphide. Moreover, the improved exposure of catalytically active sites on the surface enhances the efficiency during OER, which is attributed to the spherically concomitant foamy morphology of the electrode material [31,44].

3.3.2. Hydrogen evolution reaction

The HER catalytic activities of the prepared SCFN and N-CNF electrodes were executed by the LSV analysis in the negative potential range of 0 to −0.6 V (vs RHE) in 1 M KOH electrolyte at 5 mV s^{-1} and are shown in Fig. 5a. Among these, the onset potential of N-CNF electrocatalyst was −0.11 V (vs RHE) with an overpotential of 160 mV to achieve a current density of 10 mA cm^{-2} for HER activity. However, the overpotential of N-CNF is comparatively higher side than the commercial Pt/C electrocatalysts (130 mV) to attain the same current density. The prepared N-CNF electrocatalyst offered a relatively enhanced HER activity compared to the reported HER electrocatalyst listed in Table 1. Fig. 5b illustrates the HER overpotentials required by the prepared electrocatalysts to achieve a current density of 10 mA cm^{-2} and the corresponding Tafel plot is presented in Fig. 5c. Mostly, the possible reaction steps of HER under alkaline conditions follow the Volmer–Heyrosky-Tafel mechanism that it involves a discharge reaction (b ≈ 120 mV/dec), followed by electrochemical desorption (b ≈ 40 mV/dec) and recombination reaction (b ≈ 30 mV/dec). In the case of N-CNF electrocatalyst, a Tafel slope of 119 mV dec^{-1} is obtained, and hence the discharge reaction is deemed to be the rate-determining step for hydrogen evolution. Fig. 5d shows the measured CA analysis of the N-CNF electrode at a constant potential of −0.28 V (vs RHE) for 25 h. It can be seen that the slight rise in current with respect to time, rather than a drop with the continuous evolution of H_2 bubbles from the electrocatalyst elucidates the excellent electrocatalytic properties. This improved HER performance of the N-CNF electrode is mainly due to the presence of various nitrogen moieties and the degree of graphitization of carbon, which are the essential parameters for HER reactions. Pyridinic and graphitic nitrogen in the carbon frame is recognised to stimulate asymmetry in charge distribution around their adjacent carbon atoms and attain an ideal value of Gibbs free-energy for hydrogen adsorption (|ΔGH*|) [51]. Thus, the N-dopants can synergistically co-activate the neighbouring carbon atoms, leading to more active catalytic sites for HER [52]. Meanwhile, the decidedly graphitized carbon background also facilitates the electron transfer process during the evolution reaction.

3.4. Electrochemical capacitive properties of the prepared electrodes

3.4.1. SCFN as a positive electrode for supercapatteries

The electrochemical properties were studied by a conventional three-electrode system involving the prepared SCFN as a working electrode (1 × 1 cm^2), a graphite rod as an auxiliary electrode (1 × 1 cm^2) and a Hg/HgO as a reference electrode. The cyclic voltammetry (CV) curves of the SCFN electrode at a different scan rates from 1 to 10 mV s^{-1} with a potential range from 0 to 0.6 V (vs Hg/HgO) is shown in Fig. 6a. The observed pair of redox peaks in the SCFN electrode reveals the battery-like charge storage behaviour [6]. The anodic and cathodic peaks give the impression to be much broader than they usually exist and the peaks corresponding to the communal oxidation and reduction reactions of Co and Ni atoms on the surface of the electrode. The corresponding Faradaic electrochemical reaction involved as follows [7,53,54].

$$NiCoP + 2OH^- \leftrightarrow NiCoP(OH^-)_2 + 2e^- \quad (1)$$

The calculated specific capacitance at 1 mV s^{-1} is 1477 F g^{-1}.

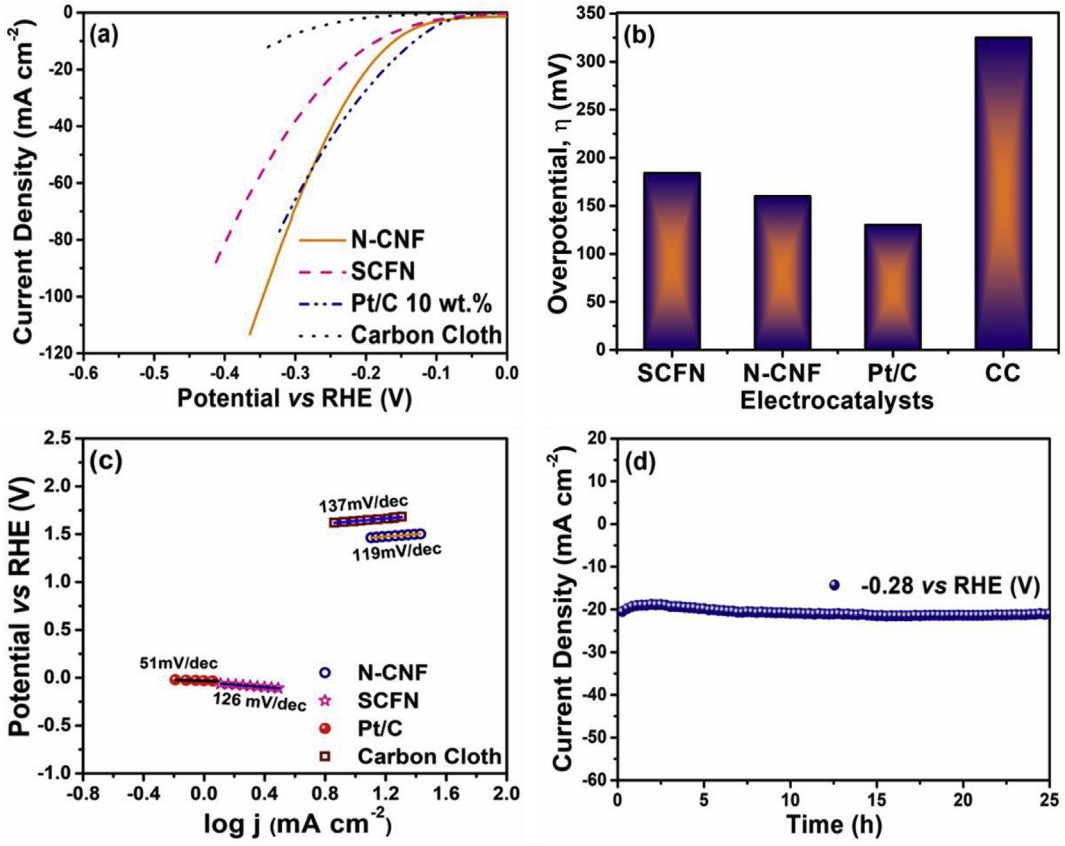

Fig. 5. (a) LSV polarization curves for HER, (b) The necessary overpotential to achieve a current density of 10 mA cm^{-2} for different electrocatalysts, (c) Corresponding HER Tafel plots and (d) Chronoamperometry of N-CNF.

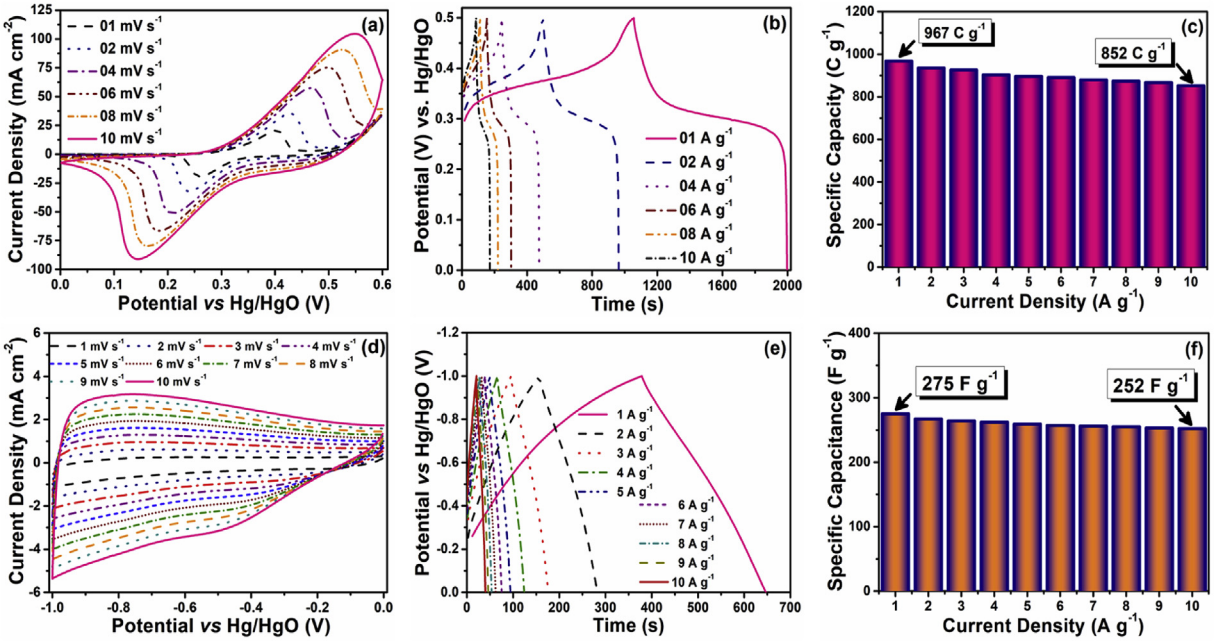

Fig. 6. (a) CV curves of SCFN with different scan rates, (b) GCD curves of SCFN with different current densities, (c) Current density vs Specific capacity plot of SCFN electrode, (d) CV curves of N-CNF with different scan rate, (e) GCD curves of N-CNF with different current densities, and (f) Current density vs Specific capacitance plot of N-CNF.

Fig. S2 shows that the anodic and cathodic peak current increases with the square root of scan rate (1–10 mV s^{-1}), which agrees well with the Randles-Sevick equation with an adjacent R-square value of 0.999 and 0.999, respectively, revealing that the process is under a diffusion-controlled system [55,56]. Fig. 6b shows the galvanostatic charge-discharge (GCD) curves of the SCFN electrode at different current densities from 1 to 10 Ag^{-1}. Substantiating the CV results, the GCD curves also transpire the battery behaviour of the SCFN electrode through the incidence of the plateau-like region. The calculated specific capacity of SCFN electrode is 967 C g^{-1} (1935 F g^{-1} or 269 mAh g^{-1}) at 1 A g^{-1} [57–59]. The accomplished extraordinary specific capacity of the SCFN electrode surpasses the reported NiCoP based electrodes with a huge margin as tabulated in Table 2 [21–24]. The obtained high specific capacity of the SCFN electrode may be attributed to the foamy nature of the material. Also, the spherically concomitant particles possess substantial orifices at their junctures that anticipates the ions to penetrate into it, generating upsurge exposure of the electrode materials from the surface to the depth. As a result, a massive volume of ions gets occupied in the orifices on the surface of the electrode that enhances the capacity of the electrode to a greater extent. Hence, the natural existence of these orifices is well-thought-out to be more than a benefit, which is liable to the high specific capacity accomplished by the SCFN electrode. Fig. 6c displays the specific capacity retention of the prepared SCFN electrodes which has delivered a high specific capacity of 852 C g^{-1}, by upholding 88% of its initial specific capacity even at a high current density of 10 Ag^{-1}. Further, to investigate the stability of the SCFN electrode, the cyclic life tests were carried out for 6000 cycles at a constant current density of 10 Ag^{-1} in Fig. S3. It reveals that the SCFN electrode performs a steady state behaviour throughout the cycle life with a negligible loss of its initial specific capacity. Fig. S4 shows the EIS spectrum of SCFN electrode with its equivalent circuit. The obtained parameters from the equivalent circuit are given in Table S1. The diameter of the semi-circle at high frequency is very much smaller around 1.4 Ω. It infers the enhanced conductivity of the prepared SCFN that accounts for the faster reaction kinetics of the electrode [60,61].

3.4.2. N-CNF as a negative electrode for supercapatteries

As reported to the above positive electrode, the similar assessments were carried out for the prepared N-CNF as a negative electrode. Fig. 6d represents the CV curves obtained at different scan rate with a potential ranging from 0 to −1 V (vs Hg/HgO). The occurrence of the rectangular CV curves embodies the EDLC behaviour and non-faradaic charge storage mechanism of the electrode [6]. The non-Faradaic electrochemical reaction involved as follows [7].

$$\text{N-CNF} + xK^{+} + xe^{-} \leftrightarrow \text{N-CNF}\,(xe^{-}) \parallel xK^{+} \quad (2)$$

The obtained specific capacitance of the prepared negative electrode was 337 F g^{-1} at 1 mV s^{-1}. The corresponding GCD curves at different current densities in the potential range of 0 to −1.0 V (vs Hg/HgO) are shown in Fig. 6e. The observed triangular behaviour exposes the EDLC nature of the electrode material. The specific capacitance of 275 F g^{-1} at a current density of 1 Ag^{-1} was obtained

Table 2
Comparison of SCFN electrode with other NiCoP electrodes.

Materials	Substrate	Electrolyte	Capacity/Capacitance	Ref
NiCoP	Carbon Paper binder free	1 M KOH	194 mAh g^{-1} at 1 A g^{-1}	[21]
NiCoP/NF	Nickel Foam (NF)	2 M KOH	9.20 F cm^{-2} at 2 mA cm^{-2}	[22]
NiCoP/G	NiCoP/G	2 M KOH	675 at 2 A g^{-1}	[23]
NiCoP	Nickel Foam (NF)	6 M KOH	571 C g^{-1} at 1 A g^{-1}	[24]
SCNF	CC	1 M KOH	967 C g^{-1} at 1 A g^{-1}	This work

from the GCD curves. The prepared N-CNF has retained 92% of its specific capacitance at a high current density of 10 Ag^{-1} as shown in Fig. 6f. Fig. S5 shows the cyclic stability of N-CNF electrode with an improved coulombic efficiency and a negligible loss of its initial specific capacitance even after 2000 cycles. Additionally, the EIS spectrum of N-CNF electrode fitted with respect to its equivalent circuit is shown in Fig. S6. The obtained parameters from the equivalent circuit are given in Table S2. The diameter of the semi-circle at high frequency is very much smaller inferring the enhanced conductivity of the prepared N-CNF electrode [60,61].

3.5. Electrochemical properties of fabricated (SCFN||N-CNF) supercapattery

Successful exploration of both SCFN and N-CNF electrodes has persuaded to paradigm a coin-type supercapattery by separating both the electrodes with a separator bounded by an aqueous electrolyte medium and sealed as illustrated in Fig. 7a [7]. To ensure the mass balance, the mass loading of the negative electrode material is adjusted with respect to the positive electrode, and the corresponding mass ratio is ~1.5:0.5 mg. Fig. 7(b and c) shows the CV and GCD curve of the fabricated supercapattery measured in the potential range from 0 to 1.6 V. The obtained specific capacity of the device from the CV and GCD curves are 181 F g^{-1} at 10 mV s^{-1} and 189 C g^{-1} at 0.5 Ag^{-1}, respectively. Subsequently, the calculated energy densities of 56 and 42 Wh Kg^{-1} with respect to the power densities of 533 and 5333 W kg^{-1} at a current density of 0.5 and 5 Ag^{-1}, respectively. The fabricated device has seen to afford an enhanced specific capacity retention, which retains a reasonable volume of its initial specific capacity after a high current density of 5 Ag^{-1} as shown in Fig. 7d. The cyclic stability of the fabricated supercapattery was measured at the current density of 5 Ag^{-1} for about 6000 cycles (Fig. 7e). The obtained initial specific capacity (140 C g^{-1}) increases initially for ~500 cycles and reached a specific capacity of 172 C g^{-1} and further retained the specific capacity of 131 C g^{-1} for the rest of the 6000 cycles. In Fig. S7 the EIS spectrum of a fabricated device fitted to its equivalent circuit reflects with a smaller diameter of the semi-circle at higher frequency confirming faster reaction kinetics of the device was due to its improved conductivity [60,61]. The obtained parameters from the equivalent circuit are given in Table S3. The Ragone plot in Fig. 7f comprises in comparison of the prepared hybrid capacitor with reported hybrid NiCoP capacitors. The reported hybrid NiCoP capacitors show a sufficient loss of its initial power density with respect to its increase in energy density. However, our device has grabbed immense control over it. Table 3 illustrates the comparison of the fabricated device with the reported NiCoP based capacitors. It elucidates in detail the disparities of the reported and the present work with respect to the used substrate, the concentration of the electrolyte, and the device performance. From the above results, it is confirmed

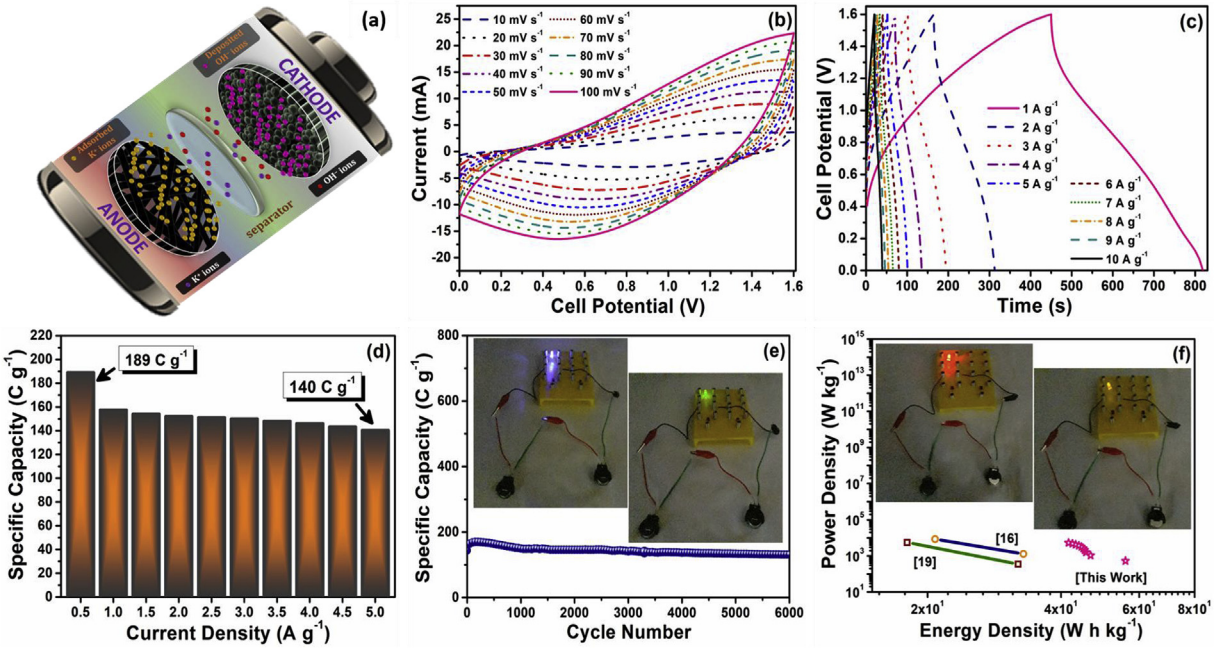

Fig. 7. (a) Schematic representation of the fabricated device, (b) CV curves of the device at various scan rates, (c) GCD curves of the device at various current densities, (d) Specific capacity vs current density plot, (e) Cycling stability for 6000 cycles, and (f) The Ragone plot comprises the Ni-based compounds reported in recent times with the current work (inset of (e) and (f) shows the real time applications of the fabricated device).

Table 3
Comparison of fabricated supercapattery with other NiCoP based capacitors.

Device materials	Substrate	Electrolyte	Cell voltage (V)	Specific capacity/ capacitance	Energy density (Wh kg^{-1})	Power density (W kg^{-1})	Ref. No.
NiCoP || Graphene films	Carbon paper binder free	1 M KOH	1.5 V	43.8 mAh g^{-1} at 2 A g^{-1}	32.9 & 20.8	1301& 8509	[21]
NiCoP/NF || Activated Carbon (AC)	Nickel foam (NF)	2 M KOH	1.6 V	3.26 F cm^{-2} at 2 mA cm^{-2}	1.16 mWhcm^{-2} at 2 mAcm^{-2}	1.6 mWcm^{-2}	[22]
NiCoP || AC	Nickel foam (NF)	6 M KOH	1.6 V	164 C g^{-1} at 0.5 A g^{-1}	32 & 18	351 & 5586	[24]
SCFN	Carbon Cloth	1 M KOH	1.6 V	189 C g^{-1} at 0.5 A g^{-1}	56 & 42	533 & 5333	This work

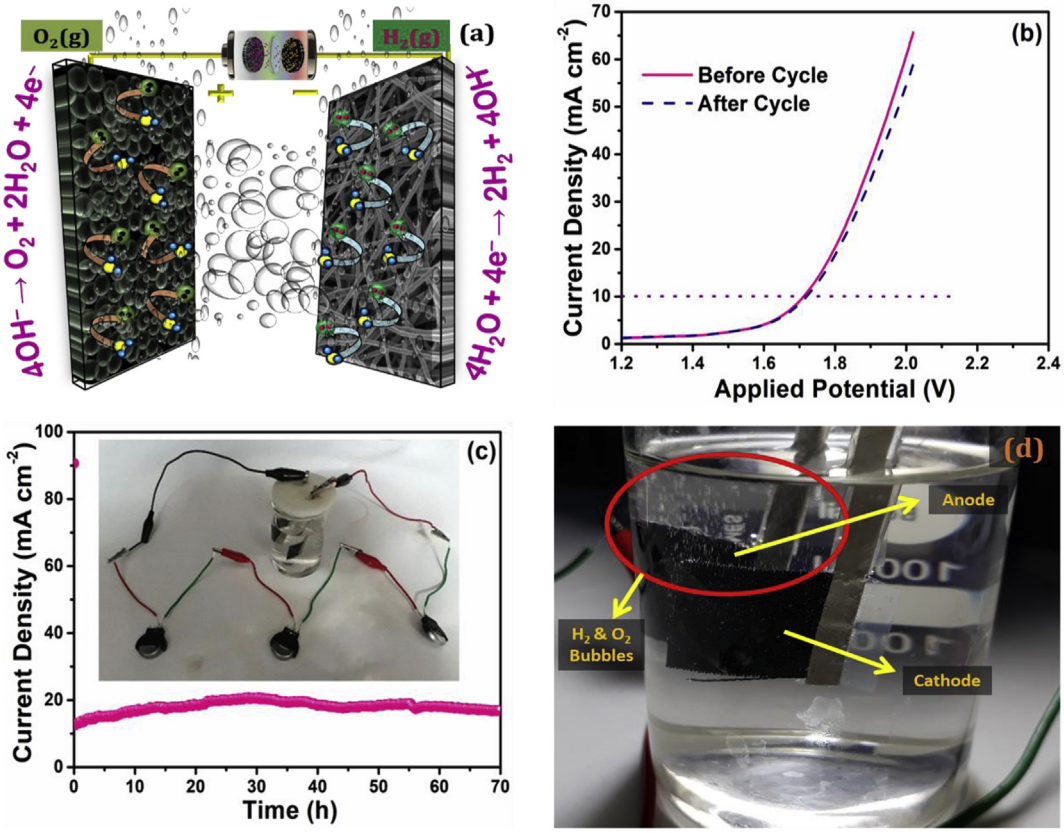

Fig. 8. (a) Schematic representation of the assembled lab-scale hybrid water electrolyser, (b) LSV polarization curves of the device before and after 70 h durability test, (c) CA curves of the device for 70 h (inset) shows the fabricated supercapattery supported water electrolyser and (d) Photographic image of the generated O_2 and H_2 bubbles obtained by self-supported water electrolyser.

that the assembled SCFN||N-CNF supercapattery with the carbon cloth substrates has provided an enhanced performance when compared to other reported capacitor devices [21,22,24].

3.6. Lab scale hybrid water electrolyser driven by fabricated supercapattery

As a result of the improved electrocatalytic activity and energy storage capability of the prepared SCFN and N-CNF electrodes, the fabricated supercapattery driven lab-scale hybrid water electrolyser was designed. The lab-scale hybrid water electrolyser was assembled by a two-electrode set up encompassing SCFN and N-CNF electrodes as anode and cathode as illustrated in Fig. 8a. Fig. 8b shows the LSV curves of the water electrolyser, which offers a minimum potential of 1.71 V to attain a current density of 10 mA cm^{-2}. The CA analysis (Fig. 8c) of the water electrolyser measured at a constant potential (1.75 V). It reveals the steady-state evolution of H_2 bubbles and resilient strength of SCFN and N-CNF electrodes further substantiated by the obtained LSV curves before and after CA analysis with no significant differences. Inset of Fig. 8c exhibits the designed water electrolyser powered by three fabricated coin-type supercapatteries. Fig. 8d portraits the O_2 and H_2 bubbles generated by the proposed supercapattery driven water electrolyser.

4. Conclusions

Here, a simplistic electrospinning technique is used to develop an encouraging nitrogen-doped carbon nanofiber (N-CNF) as a negatrode, while a facile single-step hydrothermal technique is implemented to propose a unique bimetallic nickel cobalt phosphides as a positrode. The prepared electrodes were keenly scrutinised through the basic electrochemical characterizations of both the energy conversion and energy storage systems. The SCFN and the N-CNF electrodes embolden a superior OER (257 mV) and HER (160 mV) electrocatalytic activity, respectively. Also, both the electrodes expressed an enhanced energy storage capacity with a remarkable rate capability and resilient cycling stability. Overall, a coin-type supercapattery (SCFN||N-CNF) was fabricated providing an astounding energy density (56 Wh kg^{-1}) and an improved power density (5333 W kg^{-1}). The fabricated storage device was integrated with an assembled hybrid water electrolyser (SCFN||N-CNF) and demonstrated. The proposed supercapattery driven hybrid water electrolyser system demanded a low cell voltage of 1.71 V to afford a high current density of 10 mA cm^{-2}. Overall, it can be concluded that the prepared SCFN and N-CNF electrodes profoundly proved its superiority of handling the multifunctional challenges in terms of both supercapattery and water electrolyser.

Acknowledgement

Dr R. Kalai Selvan would like to thank University Grants Commission (UGC), India for awarding Raman Post-Doctoral Fellowship to carry out the part of this work (N-CNF preparation) at NC State University, USA. The part of the work (XRD, XPS and FESEM analysis of N-CNF samples) was performed in the Analytical Instrumentation Facility (AIF) at North Carolina State University, USA. Prof. Yun Sung Lee acknowledges the Ministry of Science, ICT and Future

Planning of South Korea for providing a National Research Foundation of Korea (NRF) grant (No. 2016R1A4A1012224).

Appendix A. Supplementary data

Supplementary data to this article can be found online at https://doi.org/10.1016/j.electacta.2018.11.078.

References

[1] C. Hu, L. Dai, Multifunctional carbon-based metal-free electrocatalysts for simultaneous oxygen reduction, oxygen evolution, and hydrogen evolution, Adv. Mater. 29 (2017), 1604942.

[2] C. Wang, J. Jiang, T. Ding, G. Chen, W. Xu, Q. Yang, Monodisperse ternary NiCoP nanostructures as a bifunctional electrocatalyst for both hydrogen and oxygen evolution reactions with excellent performance, Adv. Mater. Interfaces 3 (2016), 1500454.

[3] A. Sivanantham, P. Ganesan, S. Shanmugam, Hierarchical $NiCo_2S_4$ nanowire arrays supported on Ni foam: an efficient and durable bifunctional electrocatalyst for oxygen and hydrogen evolution reactions, Adv. Funct. Mater. 26 (2016) 4661–4672.

[4] M.S. Burke, L.J. Enman, A.S. Batchellor, S. Zou, S.W. Boettcher, Oxygen evolution reaction electrocatalysis on transition metal oxides and (oxy)hydroxides: activity trends and design principles, Chem. Mater. 27 (2015) 7549–7558.

[5] Z. Zhang, S. Liu, J. Xiao, S. Wang, Fiber-based multifunctional nickel phosphide electrodes for flexible energy conversion and storage, J. Mater. Chem. A 4 (2016) 9691–9699.

[6] S.T. Senthilkumar, R. Kalai Selvan, Flexible fiber supercapacitor using biowaste-derived porous carbon, ChemElectroChem 2 (2015) 1111–1116.

[7] B. Senthilkumar, Z. Khan, S. Park, K. Kim, H. Ko, Y. Kim, Highly porous graphitic carbon and $Ni_2P_2O_7$ for a high performance aqueous hybrid supercapacitor, J. Mater. Chem. A 3 (2015) 21553–21561.

[8] R. Li, X. Ba, H. Zhang, P. Xu, Y. Li, C. Cheng, J. Liu, Conformal multifunctional titania shell on iron oxide nanorod conversion electrode enables high stability exceeding 30 000 cycles in aqueous electrolyte, Adv. Funct. Mater. 28 (2018), 1800497.

[9] L. Hui, Y. Xue, D. Jia, H. Yu, C. Zhang, Y. Li, Multifunctional single-crystallized carbonate hydroxides as highly efficient electrocatalyst for full water splitting, Adv. Energy Mater. 8 (2018), 1800175.

[10] J.G.-D.-L.-. Rosa, L.G. Arriaga, A. Álvarez, N. Arjona, A. Déctor, A.U.C.- Ramírez, V.V.- Becerra, J.L.- García, NiAl layered double hydroxides and PdNiO as multifunctional anodes for prospective self-powered lab-on-a-chip dopamine sensors, ChemNanoMat 4 (2018) 688–697.

[11] I.K. Durga, S.S. Rao, A.E. Reddy, C.V.V.M. Gopi, H.-J. Kim, Achieving copper sulfide leaf-like nanostructure electrode for high-performance supercapacitor and quantum-dot-sensitized solar cells, Appl. Surf. Sci. 435 (2018) 666–675.

[12] X. Cao, D. Jia, D. Li, L. Cui, J. Liu, One-step co-electrodeposition of hierarchical radial NixP nanospheres on Ni foam as highly active flexible electrodes for hydrogen evolution reaction and supercapacitor, Chem. Eng. J. 348 (2018) 310–318.

[13] Y. Xu, S. Hou, G. Yang, X. Wang, T. Lu, L. Pan, Synthesis of bimetallic $Ni_xCo_{1-x}P$ hollow nanocages from metal-organic frameworks for high-performance hybrid supercapacitors, Electrochim. Acta 285 (2018) 192–201.

[14] X.-W. Wang, H.-P. Guo, J. Liang, J.-F. Zhang, B. Zhang, J.-Z. Wang, W.-B. Luo, H.-K. Liu, S.-X. Dou, An integrated free-standing flexible electrode with Holey-structured 2D bimetallic phosphide nanosheets for sodium-ion batteries, Adv. Funct. Mater. 28 (2018), 1801016.

[15] Y. Du, Z. Li, Y. Liu, Y. Yang, L. Wang, Nickel-iron phosphides nanorods derived from bimetallic-organic frameworks for hydrogen evolution reaction, Appl. Surf. Sci. 457 (2018) 1081–1086.

[16] C. Du, L. Yang, F. Yang, G. Cheng, W. Luo, Nest-like NiCoP for highly efficient overall water splitting, ACS Catal. 7 (2017) 4131–4137.

[17] J. Li, G. Wei, Y. Zhu, Y. Xi, X. Pan, Y. Ji, I.V. Zatovsky, W. Han, Hierarchical NiCoP nanocone arrays supported on Ni foam as an efficient and stable bifunctional electrocatalyst for overall water splitting, J. Mater. Chem. A 5 (2017) 14828–14837.

[18] H. Liang, A.N. Gandi, D.H. Anjum, X. Wang, U. Schwingenschlogl, H.N. Alshareef, Plasma-assisted synthesis of NiCoP for efficient overall water splitting, Nano Lett. 16 (2016) 7718–7725.

[19] J. Yu, Q. Li, Y. Li, C. Xu, L. Zhen, V. Dravid, J. Wu, Ternary metal phosphide with triple-layered structure as a low-cost and efficient electrocatalyst for bifunctional water splitting, Adv. Funct. Mater. 26 (2016) 7644–7651.

[20] J. Li, M. Yan, X. Zhou, Z.Q. Huang, Z. Xia, C.R. Chang, Y. Ma, Y. Qu, Mechanistic insights on ternary $Ni_{2-x}Co_xP$ for hydrogen evolution and their hybrids with graphene as highly efficient and robust catalysts for overall water splitting, Adv. Funct. Mater. 26 (2016) 6785–6796.

[21] H. Liang, C. Xia, Q. Jiang, A.N. Gandi, U. Schwingenschlogl, H.N. Alshareef, Low-temperature synthesis of ternary metal phosphides using plasma for asymmetric supercapacitors, Nanomater. Energy 35 (2017) 331–340.

[22] M. Kong, Z. Wang, W. Wang, M. Ma, D. Liu, S. Hao, R. Kong, G. Du, A.M. Asiri, Y. Yao, X. Sun, NiCoP nanoarray: a superior pseudocapacitor electrode with high areal capacitance, Chem. Eur J. 23 (2017) 4435–4441.

[23] C. Wang, Y. Qian, J. Yang, S. Xing, X. Ding, Q. Yang, Ternary NiCoP nanoparticles assembled on graphene for high-performance lithium-ion batteries and supercapacitors, RSC Adv. 7 (2017) 26120–26124.

[24] Y. Hu, M. Liu, Y. Hu, Q. Yang, L. Kong, L. Kang, One-pot hydrothermal synthesis of porous nickel cobalt phosphides with high conductivity for advanced energy conversion and storage, Electrochim. Acta 215 (2017) 114–125.

[25] S. Surendran, S. Shanmugapriya, A. Sivanantham, S. Shanmugam, R. Kalai Selvan, Electrospun carbon nanofibers encapsulated with NiCoP: a multifunctional electrode for supercapattery and oxygen reduction, oxygen evolution, and hydrogen evolution reactions, Adv. Energy Mater. 8 (2018), 1800555.

[26] L. Chen, Y. Feng, H. Liang, Z. Wu, S. Yu, Macroscopic-scale three-dimensional carbon nanofiber architectures for electrochemical energy storage devices, Adv. Energy Mater. 7 (2017), 1700826.

[27] X. Lu, C. Wang, F. Favier, N. Pinna, Electrospun nanomaterials for supercapacitor electrodes: designed architectures and electrochemical performance, Adv. Energy Mater. 7 (2017), 1601301.

[28] Z. Donga, S.J. Kennedy, Y. Wu, Electrospinning materials for energy-related applications and devices, J. Power Sources 196 (2011) 4886–4904.

[29] J. Lai, A. Nsabimana, R. Luque, G. Xu, 3D porous carbonaceous electrodes for electrocatalytic applications, Joule 2 (2018) 76–93.

[30] J. Zhu, C. Chen, Y. Lu, Y. Ge, H. Jiang, K. Fu, X. Zhang, Nitrogen-doped carbon nanofibers derived from polyacrylonitrile for use as anode material in sodium-ion batteries, Carbon 94 (2015) 189–195.

[31] X. Wang, R. Tong, Y. Wang, H. Tao, Z. Zhang, H. Wang, H. Wang, Surface roughening of nickel-cobalt phosphide nanowire arrays/Ni foam for enhanced hydrogen evolution activity, ACS Appl. Mater. Interfaces 8 (2016) 34270–34279.

[32] T. Liu, X. Yan, P. Xi, J. Chen, D. Qin, D. Shan, S. Devaramani, X. Lu, X. Lu, Nickel–Cobalt phosphide nanowires supported on Ni foam as a highly efficient catalyst for electrochemical hydrogen evolution reaction, Int. J. Hydrogen Energy 42 (2017) 14124–14132.

[33] L. Roldán, S. Armenise, Y. Marco, E. García-Bordeje, Control of nitrogen insertion during the growth of nitrogen-containing carbon nanofibers on cordierite monolith walls, Phys. Chem. Chem. Phys. 14 (2012) 3568–3575.

[34] B. Kumar, M. Asadi, D. Pisasale, S. Sinha-Ray, B.A. Rosen, R. Haasch, J. Abiade, A.L. Yarin, A. Salehi-Khojin, Renewable and metal-free carbon nanofibre catalysts for carbon dioxide reduction, Nat. Commun. 4 (2013) 2819.

[35] Q. Yao, B. Fan, Y. Xiong, C. Jin, Q. Sun, C. Sheng, 3D assembly based on 2D structure of cellulose nanofibril/graphene oxide hybrid aerogel for adsorptive removal of antibiotics in water, Sci. Rep. 7 (2017) 45914.

[36] G.C. Marjanović, I. Pašti, S. Mentus, One-dimensional nitrogen-containing carbon nanostructures, Prog. Mater. Sci. 69 (2015) 61–182.

[37] R. Li, X. Li, J. Chen, J. Wang, H. He, B. Huang, Y. Liu, Y. Zhou, G. Yang, Pyridinic-nitrogen-highly doping nanotubular carbon arrays grown on carbon cloth for high performance and flexible supercapacitors, Nanoscale 10 (2018) 3981–3989.

[38] F. Davodi, M. Tavakkoli, J. Lahtinen, T. Kallio, Straight forward synthesis of nitrogen-doped carbon nanotubes as highly active bifunctional electrocatalysts for full water splitting, J. Catal. 353 (2017) 19–27.

[39] B. Zou, Y. Gao, B. Liu, Y. Yu, Y. lu, Three-dimensional heteroatom-doped carbon composite film for flexible solid-state supercapacitors, RSC Adv. 6 (2017) 4483–4489.

[40] C. Zhan, Q. Xu, X. Yu, Q. Liang, Y. Bai, Z. Huang, F. Kang, Nitrogen-rich hierarchical porous hollow carbon nanofibers for high-performance supercapacitor electrodes, RSC Adv. 6 (2016) 41473–41476.

[41] X. Zou, X. Huang, A. Goswami, R. Silva, B.R. Sathe, E. Mikmekov, T. Asefa, Cobalt-embedded nitrogen-rich carbon nanotubes efficiently catalyze hydrogen evolution reaction at all ph values, Angew. Chem. 126 (2014) 4461–4465.

[42] Z. Yin, C. Zhu, C. Li, S. Zhang, X. Zhang, Y. Chen, Hierarchical nickel–cobalt phosphide yolk–shell spheres as highly active and stable bifunctional electrocatalysts for overall water splitting, Nanoscale 8 (2016) 19129–19138.

[43] Y. Li, H. Zhang, M. Jiang, Y. Kuang, X. Sun, X. Duan, Ternary NiCoP nanosheet arrays: an excellent bifunctional catalyst for alkaline overall water splitting, Nano Research 9 (2016) 2251–2259.

[44] Y. Bai, H. Zhang, L. Liu, H. Xu, Y. Wang, Tunable and specific formation of C@NiCoP peapods with enhanced her activity and lithium storage performance, Chem. Eur J. 22 (2016) 1021–1029.

[45] L. Ye, Z. Wen, Reduced graphene oxide supporting hollow bimetallic phosphide nanoparticle hybrids for electrocatalytic oxygen evolution, Electrochem. Commun. 83 (2017) 85–89.

[46] X. Zhang, L. Huang, Q. Wang, S. Dong, Transformation of homobimetallic MOFs into nickel–cobalt phosphide/nitrogen-doped carbon polyhedral nanocages for efficient oxygen evolution electrocatalysis, J. Mater. Chem. A 5 (2017) 18839–18844.

[47] Y. Li, Z. Jiang, J. Huang, X. Zhang, J. Chen, Template-synthesis and electrochemical properties of urchin-like NiCoP electrocatalyst for hydrogen evolution reaction, Electrochim. Acta 249 (2017) 301–307.

[48] L. Han, T. Yu, W. Lei, W. Liu, K. Feng, Y. Ding, G. Jiang, P. Xu, Z. Chen, Nitrogen-doped carbon nanocones encapsulating with nickel-cobalt mixed phosphides for enhanced hydrogen evolution reaction, J. Mater. Chem. A 5 (2017) 16568–16572.

[49] Y. Li, J. Liu, C. Chen, X. Zhang, J. Chen, Preparation of NiCoP hollow quasi-polyhedra and their electrocatalytic properties for hydrogen evolution in

alkaline solution, ACS Appl. Mater. Interfaces 9 (2017) 5982–5991.
[50] Y. Li, Y. Tian, Y. Yan, H. Chang, R. Ouyang, Y. Miao, NiCoP nanoparticles as efficient electrocatalyst for oxygen evolution reaction in an alkaline solution, Int. J. Electrochem. Sci. 11 (2016) 9917–9927.
[51] D.K. Singh, R.N. Jenjeti, S. Sampath, M. Eswaramoorthy, Two in one: N-doped tubular carbon nanostructure as an efficient metal-free dual electrocatalyst for hydrogen evolution and oxygen reduction reactions, J. Mater. Chem. A 5 (2017) 6025–6031.
[52] H. Wang, C. Sun, Y. Cao, J. Zhu, Y. Chen, J. Guo, J. Zhao, Y. Sun, G. Zou, Molybdenum carbide nanoparticles embedded in nitrogen-doped porous carbon nanofibers as a dual catalyst for hydrogen evolution and oxygen reduction reactions, Carbon 114 (2017) 628–634.
[53] S. Surendran, S. Shanmugapriya, S. Shanmugam, L. Vasylechko, R. Kalai Selvan, Interweaved nickel phosphide sponge as an electrode for flexible supercapattery and water splitting applications, ACS Appl. Energy Mater. 1 (2018) 78–92.
[54] S. Surendran, R.K. Selvan, Growth and characterization of 3D flower-like β-NiS on carbon cloth: a dexterous and flexible multifunctional electrode for supercapattery and water-splitting applications, Adv. Mater. Interfaces 5 (2018), 1701056.
[55] J. Liu, J. Wang, Z. Ku, H. Wang, S. Chen, L. Zhang, J. Lin, Z.X. Shen, Aqueous rechargeable alkaline $CoxNi_{2-x}S_2/TiO_2$ battery, ACS Nano 10 (2016) 1007–1016.
[56] J. Liu, M. Chen, L. Zhang, J. Jiang, J. Yan, Y. Huang, J. Lin, H.J. Fan, Z.X. Shen, A flexible alkaline rechargeable Ni/Fe battery based on graphene foam/carbon nanotubes hybrid film, Nano Lett. 14 (2014) 7180–7187.
[57] P. Simon, Y. Gogotsi, B. Dunn, Where do batteries end and supercapacitors begin? Science 343 (2014) 1210–1211.
[58] Y. Gogosti, P. Simon, True performance metrics in electrochemical energy storage, Science 334 (2011) 917–918.
[59] Y. Gogosti, What nano can do for energy storage, ACS Nano 8 (2014) 5369–5371.
[60] G.K. Veerasubramani, Y. Subramanian, M.-S. Park, G. Nagaraju, B. Senthilkumar, Y.-S. Lee, D.-W. Kim, Enhanced storage ability by using a porous pyrrhotite@N-doped carbon yolk–shell structure as an advanced anode material for sodium-ion batteries, J. Mater. Chem. A 6 (2018) 20056–20068.
[61] S. Manoharan, S. Sahoo, P. Pazhamalai, S.J. Kim, Supercapacitive properties of activated carbon electrode using ammonium based proton conducting electrolytes, Int. J. Hydrogen Energy 43 (2018) 1667–1674.